

Alpha-event and surface characterisation in segmented true-coaxial HPGe detectors

I. Abt^a, L. Garbini^{a,*}, C. Gooch^a, S. Irlbeck^a, X. Liu^a, M. Palermo^{a,1}, O. Schulz^a

^a*Max-Planck-Institut für Physik, Munich, Germany*

Abstract

A detailed study of alpha interactions on the passivation layer on the end-plate of a true-coaxial high-purity germanium detector is presented. The observation of alpha events on such a surface indicates an unexpectedly thin so-called “effective dead layer” of less than $20\ \mu\text{m}$ thickness. In addition, the influence of the metalisation close to the end-plate on the time evolution of the output pulses is discussed. The results indicate that alpha contamination can result in events which could be mistaken as signals for neutrinoless double beta decay and provide some guidance on how to prevent this.

Keywords: HPGe detectors, position-sensitive devices, neutrinoless double-beta decay, background-reduction techniques

1. Introduction

The search for neutrinoless double-beta ($0\nu\beta\beta$) decay is one of the most promising approaches to look for physics beyond the standard model. The germanium isotope ^{76}Ge is one of the candidates for such a search. The current generation of germanium experiments, GERDA [1] and the MAJORANA demonstrator [2], are already setting significant limits on the half-life of ^{76}Ge for $0\nu\beta\beta$ decay [3, 4] and are working hard to push the currently available technologies to reduce the background. Recently, the GERDA collaboration has presented limits on the half-life of 5.2×10^{25} y and on the mass of the coherent Majorana state, m_{ee} , between 160 and 400 meV, depending on the nuclear matrix element used. A background index of $\approx 10^{-3}$ counts/keV/kg/y was also presented. A commonly accepted goal is to increase the sensitivity down to 10 meV in order to cover the parameter space associated with the inverted hierarchy [5]. This requires a ton-scale experiment with a background index of better than 10^{-4} counts/keV/kg/y [6].

Similar considerations lead also to the desire to build a ton-scale germanium experiment to search for dark matter [7, 8, 9]. While true-coaxial detectors are not candidates for such experiments, the relevant detectors still have passivated or oxydised surfaces and alpha interactions are relevant.

The choice of detector technology for any ton-scale experiment needs careful consideration. The study presented here provides some input to the decision making process. Large coaxial detectors are candidates for experiments searching for $0\nu\beta\beta$ decay because they can be built with masses of more than 2 kg. However, they have at least one floating end-plate, which is usually passivated. Any contamination of these end-plates with alpha emitters has to be considered [10]. Several hundred large detectors are required to achieve the necessary mass and thus the detector technology should be commercially available. Therefore, it is important to investigate detectors which are based on such technology.

*Corresponding Author

Email address: luciagarbini86@gmail.com (L. Garbini)

¹Now at Physics and Astronomy Department, University of Hawaii at Manoa, HI, US

The detector used for the study presented here was manufactured by Canberra France, now Mirion technology. It has a standard end-plate geometry, but a special segmentation to facilitate the characterisation of the end-plate. Data are presented for which the passivated top surface was scanned with a ^{241}Am source. It is shown that alpha particles are observed, even though their range in germanium is less than $30\ \mu\text{m}$. The events induced by the alpha particles are characterised. The events are influenced by a so-called “inactive” or “dead layer” underneath the passivated surface. The simplistic term “dead layer”, which is commonly used [11, 12, 13, 14], does not reflect what happens inside the detector. The actual physics of this region is involved; this region is neither inactive nor dead. Throughout this paper, the term “effective dead layer” is used. The thickness of this layer is derived by converting the energy, which could not be observed, to the thickness of a layer of germanium, which an alpha particle would have to traverse to lose the same amount of energy. As this apparent thickness can at least be partly due to charge trapping along the drift paths, it can be different for different charge carriers.

The important question for a future large-scale experiment is whether alpha particles entering from the top of the detector can be misidentified as $0\nu\beta\beta$ events if only the energy observed through the detector core is recorded. In addition, the influence of the metalisation close to the end-plate is important. As the aluminium of the metalisation could also be a source of background [15], its influence was also investigated.

2. Experimental setup and detector

The measurements presented in this paper were performed operating the “Super-Siegfried” test-detector in the GALATEA test-facility [16, 17] shown in Fig. 1, located at the Max-Planck-Institut für Physik in Munich. GALATEA is based on a vacuum chamber in which germanium detectors can be scanned by a system of three motorised stages. Two tungsten collimators are used to focus the radiation onto the mantle and the top plate of any cylindrical detector. As the paths between the collimators and the detector are free of material, it is possible to use alpha sources.

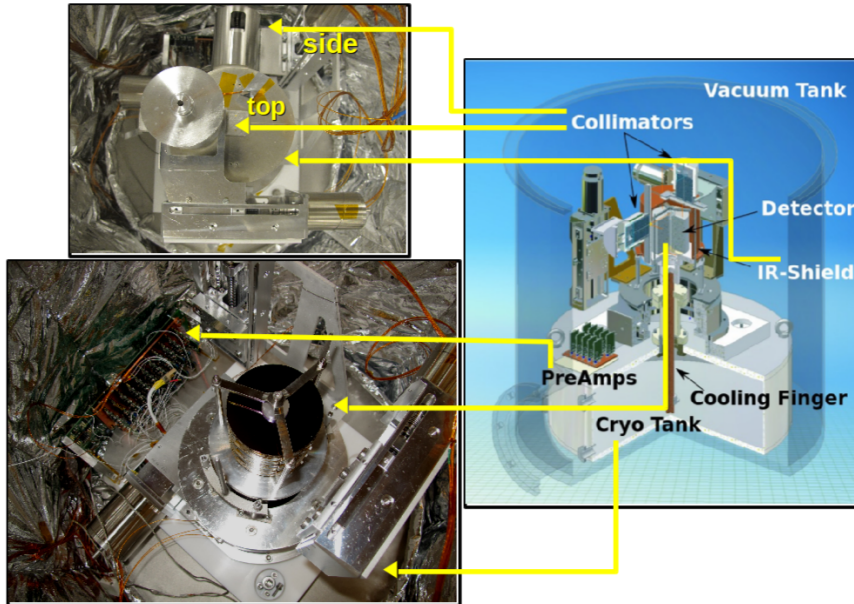


Figure 1: Operation of the Super-Siegfried detector in the GALATEA test facility, adapted from [18].

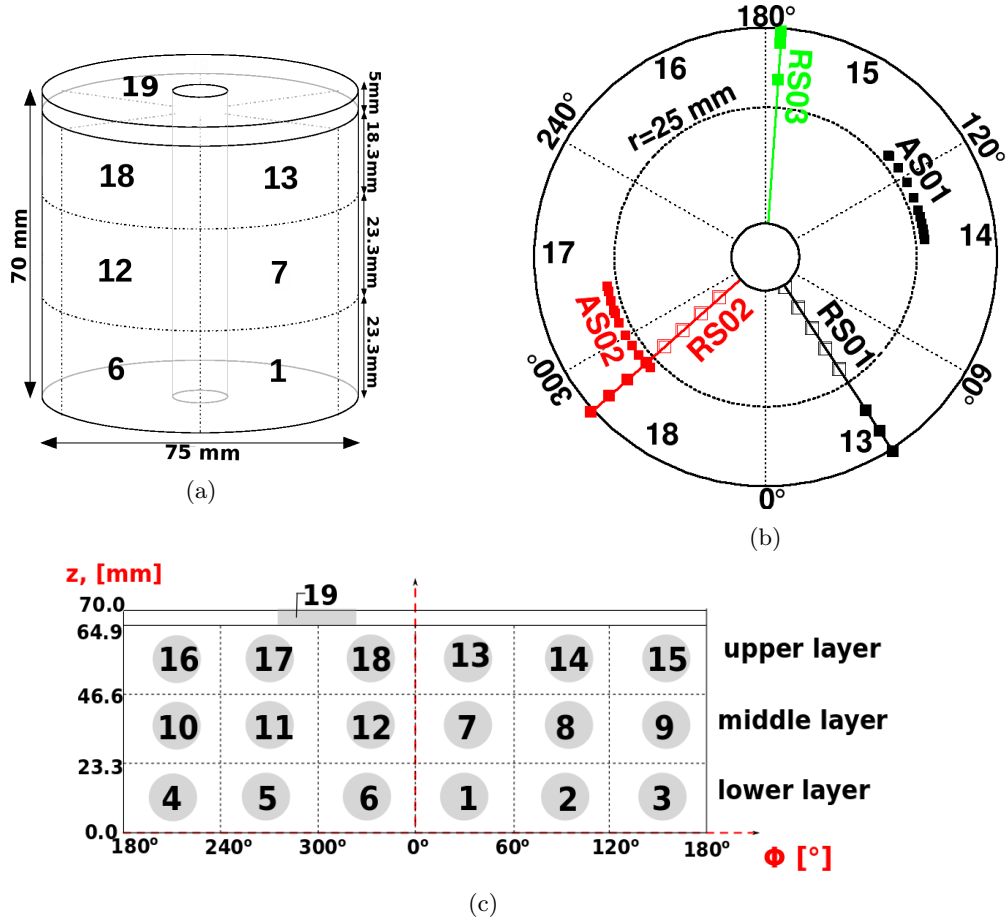


Figure 2: (a) Schematic of the 18+1 fold segmented Super-Siegrfried detector, (b) the locations of the individual measurements on the top surface. The numbers indicate the segments underneath. Open symbols indicate no observation of alpha interaction at the probed location, (c) rolled out detector mantle with dimensions and reference system. The metalised contacts are indicated as shaded areas, adapted from [18]

The data presented in this work were taken with a 10 kBq ^{241}Am source, placed inside the collimator above the top end-plate. The radius of the beam spot was 1.8 mm. Also present was a 42 kBq ^{152}Eu calibration source, located in the collimator on the side of the detector. It was moved down as far as possible in order to minimise its influence on the measurement.

The isotope ^{241}Am emits alpha particles of about 5.5 MeV. However, the source is encapsulated. Separate measurements on the side of another germanium detector, where no significant effective dead layer exists, showed that the encapsulation reduces the mean energy of the alphas to 4.5 MeV with a Gaussian variation of 0.2 MeV [18]. The variation corresponds to a 10% inhomogeneity of the thickness of the plastic encapsulation. The energy loss in germanium is 172 keV/ μm . Thus, any observation of alpha interactions indicates that the effective dead layer is thinner than 26 μm .

The ^{241}Am source also produces gamma-rays of 59.5 keV which have a mean free path in germanium of about 0.9 mm. Thus, two different volumes can be probed with one source. However, the tungsten collimator also introduces k - α emission lines at 59.3 keV and 58.0 keV which cannot be separated from the 59.5 keV gammas. They blur the beam spot such that the probed volumes not only differ in depth, but also slightly in radius.

Figure 2 shows the schematic of Super-Siegrfried and the locations of the measurements. Super-Siegrfried is a cylindrical true coaxial n-type high-purity segmented germanium detector produced by Canberra France. It has a height of 70 mm. The radius of the inner bore hole is 5.05 mm and

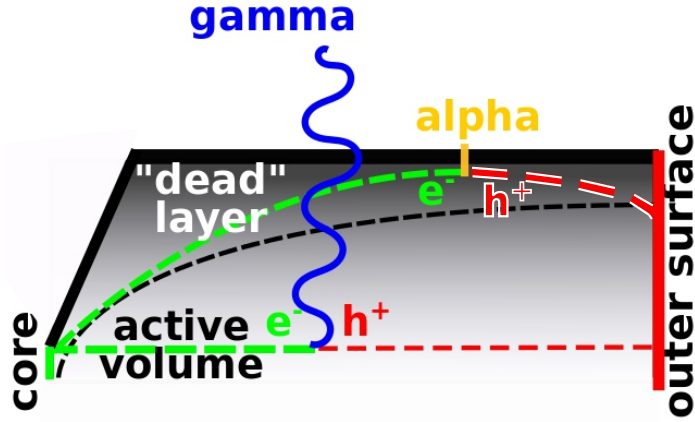


Figure 3: Vertical cut through the top of one half of the Super-Siegfried – not to scale. The central hole opens conically; the core electrode does not cover this surface. It is covered by a thin passivation layer like the top of the detector. The depth and horizontal extension of the conical hole extension are compatible to the 5 mm height of segment 19. The mantle electrode extends to almost the top of the detector, the core electrode ends a bit below the conical opening of the hole. An alpha and a gamma interaction are indicated. An effective dead layer forms underneath the passivation. At larger radii, alpha interactions are observed, even though the drift paths are not straight for charge carriers created in this region, adapted from [18]

the outer radius is 37.5 mm. According to the manufacturer, the detector has a concentration of electrically active impurities between $\rho = 0.44 \times 10^{10} \text{cm}^{-3}$ at the top and $\rho = 1.30 \times 10^{10} \text{cm}^{-3}$ at the bottom of the detector. The full depletion voltage was determined to be 2250 V. The operational voltage was 3000 V.

The main part of the detector is segmented 6-fold in ϕ and 3-fold in z . Such a detector was characterised in detail previously [19]. An additional segment, 5 mm high and not segmented in ϕ , is located above the regular 18 segments. The signals from the detector were recorded as charge pulses. Charge carriers, electrons and holes created by an energy deposition, drift towards the electrodes. The electrons drift towards the core electrode and the holes towards the segment electrodes. During the drift they induce charges which are recorded. The amount of charge registered in a given electrode at a given time depends on the amount of charge carriers drifting and the strength of the so-called weighting field of the electrode. The weighting field of the core is strong close to the centre of the detector while the weighting field of the segment electrodes is strong close to the mantle.

Super-Siegfried was previously investigated using the 122 keV ^{152}Eu line with the detector mounted in a conventional cryostat [20]. The thin top segment, called segment 19, was designed to study events on the end-plate. As it is fairly thin, any charge drifting towards the segment 19 electrode also creates strong so-called mirror pulses in the segments underneath, which facilitate a detailed pulse-shape analysis.

For each event, the pulses for the core and all 19 segments were recorded with a 75 MHz sampling rate. All pulses were corrected offline for linear cross-talk and calibrated for energy. The linear cross-talk correction of pulses was performed by using overall cross-talk factors determined on ADC level from single segment events [18]. For the core and the collecting segments, the energy was determined after calibration as the height of the respective pulse using an asymmetric trapezoidal filter. Throughout the paper, the risetime of a pulse refers to the time for the pulse to develop from 10% to 90% of its pulse height.

The metalisation of the detector was reduced in order to study its influence on the properties of the detector². Only a circular area with a radius of about 6 mm in the middle of each regular

²As aluminium is not completely radiopure a reduction of the metalisation would reduce any background from

segment was metalised, see Fig. 2(c). The metal contact of segment 19 only covered a sector of the mantle about 2 cm long.

Figure 3 depicts a schematic vertical cut through one half of segment 19. The conical shape of the bore hole and the limited extension of the core electrode by construction cause a distorted field in segment 19, i.e. the field lines cannot be horizontal. In this configuration, a not-fully depleted volume with a very weak field close to the hole is expected for purely geometrical reasons. It seems likely that charge carriers are unable to emerge from this volume.

An effect beyond simple geometry is also distorting fields in germanium detectors. In addition, space charges accumulating in the thin passivation layer and possibly oppositely charged space charges underneath can distort the field. If the field lines are bent sufficiently towards the surface, see e.g. [11], a so-called “surface channel” forms. The charge carriers can drift along these channels with significantly reduced drift speed compared to the drift speed in the unaffected bulk. Some studies using either planar detectors or assuming simpler geometries attribute all observations to surface channel effects, see e.g. [14, 12]. However, whether the field is distorted by geometry or by a space charges, the signature is a reduced speed of the charge carriers. The data presented in this paper cannot be used to distinguish between the causes.

The partial metalisation of segment 19, see Fig. 2(c), adds a further complication. It has the potential to create a phi dependence of the field, because the Boron implant is not expected to be as conductive as a standard metalisation layer. The potential on the outer layer is not as fixed as on a fully metalised detector.

The loss of observed charge can be due to charge carriers created in a volume from which they cannot emerge or due to charge trapping along their path to the electrode. The electrons drift towards the core through a region in which the weighting field of the core is much stronger than for the segment (mantle) electrode. For the holes, the situation is reversed. Their path towards the segment electrode is characterised by a strong segment weighting-field. Thus, the trapping of electrons (holes) affects predominantly the energy registered in the core (segment).

Previous measurements with ^{152}Eu [20] indicated that the effective dead layer of the detector close to the bore hole is as thick as 5 mm. These measurements were not precise enough measure the thickness of the effective dead layer at larger radii, even though they indicated that the layer was rather thin. Nevertheless, the expectations [21] for this detector were that even at larger radii, the thickness of the effective dead layer would minimally be of the order of 50 to 100 μm . A somewhat similar large-volume closed-end detector was probed with 59 keV photons and shown to have an effective dead layer on the scale of millimeters also at larger radii [13]. Thus, the observation of alpha particles on the end-plate with a range of less than 30 μm was not expected.

3. Observation of alpha radiation

Contrary to expectations, alpha interactions were consistently observed for radii larger than 25 mm. Figure 4(a) shows the spectra recorded by the core and by segment 19 for $r = 26.0$ mm and $\phi = 118^\circ$, a point covered by the AS01 scan, see Fig. 2(b). The correlation between the energies recorded in the core and in segment 19 is shown in Fig. 4(b).

Broad bumps, from now on referred to as alpha peaks, are dominating both the core and segment 19 spectra at energies above 2 MeV. The core spectrum also shows the characteristic gamma lines due to natural radioactivity and due to the ^{152}Eu source. Segment 19 is too thin to fully absorb high-energy gammas with good efficiency, but the correlation plot, Fig. 4(b), shows a thin line along the diagonal caused by single-segment 19 events. The 59 keV line is very clearly seen in both the core and segment 19 and its equal location confirms the validity of the energy calibration. Thus, the difference of the location of the alpha peaks has to be due to a different charge collection efficiency for electrons and holes. This indicates that holes must be trapped to explain the reduced energy observed on segment 19 as depicted in Fig. 4(a).

this source for low-background experiments [15].

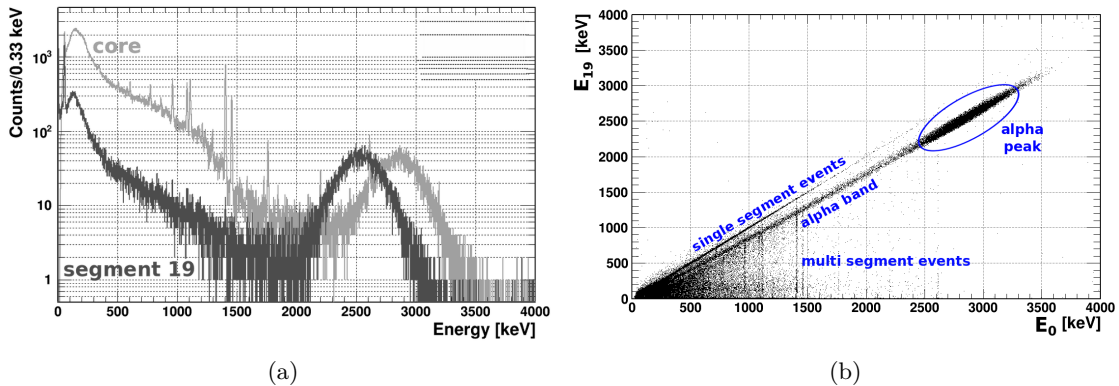


Figure 4: Observation of alpha interactions during the scan AS01, see Fig. 2(b), at $r=26.0$ mm and $\phi = 118^\circ$: (a) spectra recorded for the core and segment 19, (b) correlation between core and segment 19 energies, adapted from [18]

The band in Fig. 4(b) associated with alpha events extends down to extremely low energies. However, at low energies, multi-segment events form a background to the alpha events. At the highest energies, where the band represents the distinct alpha peaks of Fig. 4(a), basically no gamma background is present. High-energy alpha events were selected for further investigation by requiring events with core (segment 19) energies, E_0 (E_{19}) of

$$\begin{aligned} E_{min}(\alpha_0^{peak}) < E_0 < E_{max}(\alpha_0^{peak}), \\ E_{min}(\alpha_{19}^{peak}) < E_{19} < E_{max}(\alpha_{19}^{peak}), \end{aligned} \quad (1)$$

where $E_{min}(\alpha_{0(19)}^{peak})$ and $E_{max}(\alpha_{0(19)}^{peak})$ are defined as the three standard deviation differences from the mean as determined in respective Gaussian fits. The background from multi-site gamma events was measured to be much less than one percent for this selection and not considered further.

4. Charge trapping

Figure 5 depicts a typical event selected according to Eq. 1 from the measurement at $r=26$ mm and $\phi = 118^\circ$ in the AS01 set. The pulses from the core (top left), from segment 19 (top right) and from the 6 regular segments below are shown in the same time range and on the same energy scale. The lower segments only produced extremely small pulses.

The core³ and segment 19 pulses look as expected for collecting electrodes. The segment 19 pulse does not reach the height of the core pulse and it is significantly slower⁴. The core pulse shows a clear kink around 2700 ns, indicating the end of the collection of electrons. The slow rise afterwards is caused by the slow drift of holes towards the mantle. All segments in the upper layer show positive mirror pulses. As these segments do not collect any charge, the pulses should return to the baseline. This happens for segments 13, 16, 17 and 18. The pulses from segments 14 and 15, directly underneath the interaction point, however, stay above the baseline; they are so-called truncated mirror pulses, which were also described for radiation-damaged detectors [22].

Truncated mirror pulses are the signature of charge trapping. The amount of charge-trapping can be determined as the final height above the baseline at which a mirror pulse remains. This we define as the pulse-height, PH_i , of a non-collecting segment i . Adding these pulse-heights of the non-collecting segments to the energy recorded for segment 19, the energy corresponding to the core pulse can be recovered. This is demonstrated in Fig. 6 The “energy recovery” works to a level

³The pulse was inverted for easier visual comparison.

⁴The small extra peak at the start of the pulse is an artefact created by the cross-talk correction which does not take differential cross-talk from the core into segment 19 into account. Such artefacts do not influence any of the results in this paper. Differential cross-talk occurs due to the very different risetimes of the core and segment 19 pulses.

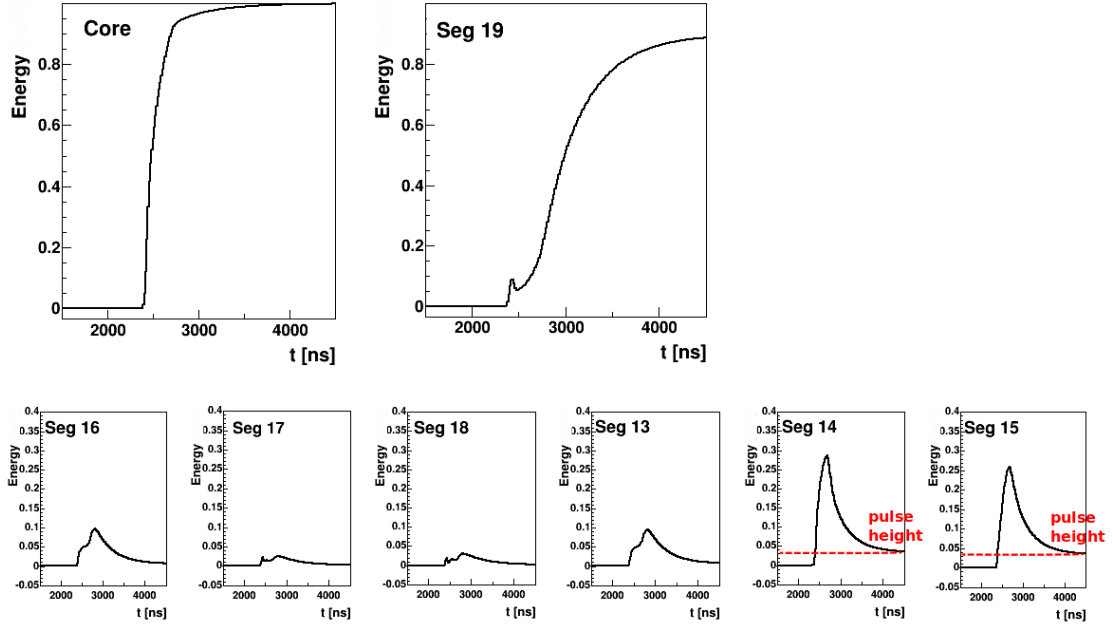


Figure 5: The pulses from the core (top left), segment 19 (top right) and the 6 regular segments below of a typical alpha event from the measurement at $r = 26.0$ mm and $\phi = 118^\circ$, in the AS01 set, close to the boundary between segments 14 and 15, adapted from [18]. All pulses are corrected for linear cross-talk. The core pulse was normalised to one; all other pulses were normalised to the core pulse, but are shown on a scale up to 0.2. The dashed lines in the segment 14 and 15 panels indicate the level at which the pulses remain above the baseline.

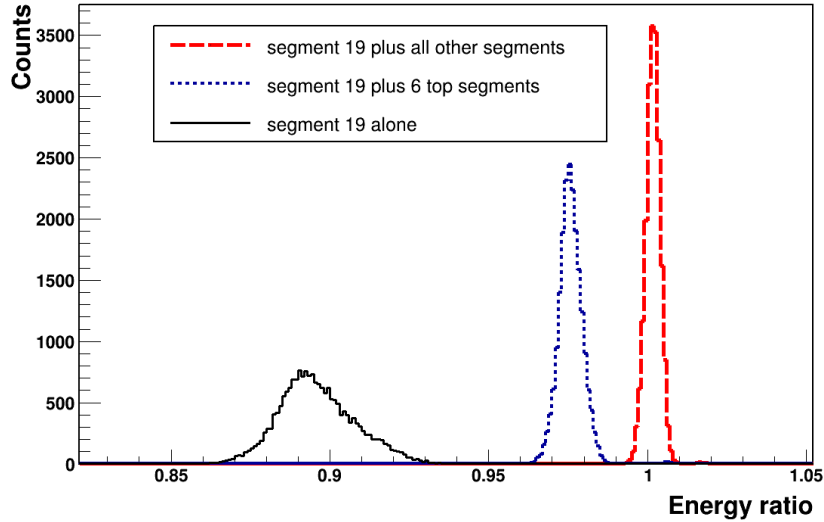


Figure 6: Distributions of the ratios E_{19}/E_0 (solid line), $(E_{19} + \sum_{i=13}^{18} PH_i)/E_0$ (dotted line) and $(E_{19} + \sum_{i=1}^{18} PH_i)/E_0$ (dashed line) for the alpha events from the measurement at $r = 26.0$ mm and $\phi = 118^\circ$, in the AS01 set, close to the boundary between segments 14 and 15.

better than 0.3% when all segments are considered. A Gaussian fit to the rightmost distribution in Fig. 6 yields a mean of 1.002 and a width of 0.25%, corresponding to less than 10 keV. Figure 6 also shows that though the mirror pulses in the lower segments are very small, they are needed to

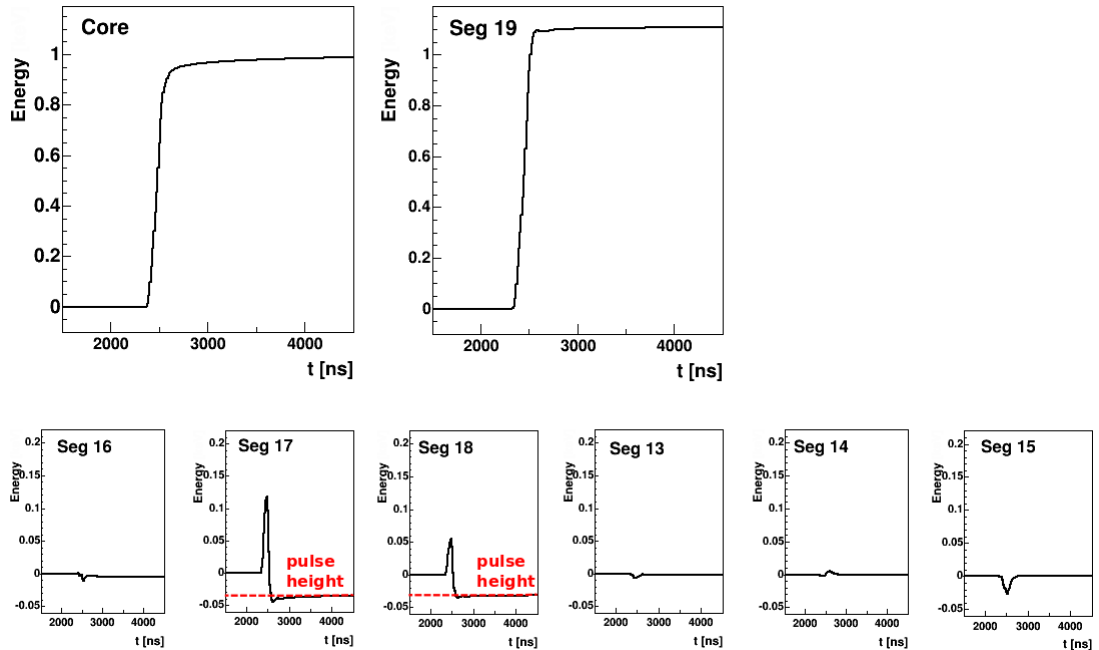


Figure 7: The pulses from the core (top left), segment 19 (top right) and the 6 regular segments below of a typical alpha event from the measurement at $r = 38.0$ mm and $\phi = 312^\circ$, in the RS02 set, close to the boundary between segments 17 and 18, adapted from [18]. All pulses are corrected for linear cross-talk. The core pulse was normalised to one; all other pulses were normalised to the core pulse, but are shown on a scale up to 0.2.

completely balance the energy.

For this source position at $r = 26.0$ mm and $\phi = 118^\circ$ in the AS01 set, 100% of the selected alpha-induced events contain such truncated positive mirror pulses; the pulses were very reproducible⁵. The segment 19 pulse has not completely flattened out at the end of the recorded time window. It is possible that some holes were released later. The time window was unfortunately limited by the data acquisition system.

The absence of negative truncated mirror pulses at this position does not exclude that also electrons are trapped. As the holes drift outwards, they come closer to the segment electrodes than the electrons and thus the large positive charge they induce makes the observation of a smaller amount of induced negative charge indicating electron trapping impossible.

The long pulse shown for segment 19 in Fig. 5 shows that the holes drift at a reduced speed. That makes them more likely to get trapped along their way to the mantle.

At larger radii, also electron trapping was observed. Figure 7 shows an event at $r = 38.0$ mm in the RS02. This event is located at the edge of the detector and close to the sector of metalisation. Figure 7 top right shows that the energy collected in segment 19 is larger than in the core and that the drift of the holes is fast in this region. The mirror pulses in segments 17 and 18 first reflect the drift of the positive holes and then the drift of the electrons. The electrons are trapped at $t \approx 2600$ ns. The other mirror pulses are much smaller. A very slow release of electrons is indicated by the slow rising tails of the mirror pulses and the steady increase of the core pulse at $t > 2600$ ns.

5. Location dependence of charge trapping

Figure 8 shows the correlation between the energy in segment 19, E_{19} , and the energy in the core, E_0 , for the three different radii probed by the RS01 set as introduced in Fig. 2(b).

⁵The somewhat unexpected reproducibility of the alpha event pulses was observed for all locations.

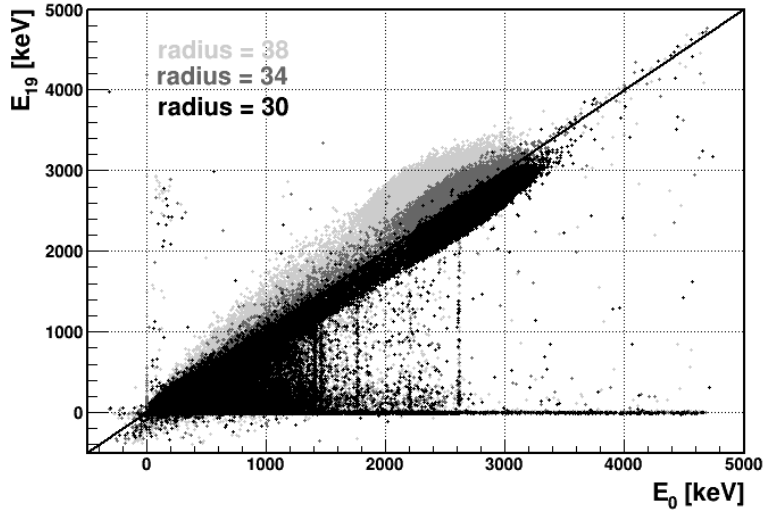


Figure 8: Correlation between E_0 and E_{19} for measurements at different radii at $\phi = 33^\circ$, RS01, see Fig. 2(b). The line along the diagonal indicates $E_0 = E_{19}$, adapted from [18].

With increasing radius, the alpha band moves from below the diagonal, normally indicating single segment events, to above. The core registers more energy for small radii and segment 19 registers more energy for large radii, close to the edge of the detector. The change in observed core energy suggests that either the really inactive volume of the detector becomes thicker towards larger radii or that also electrons get trapped. As the energy observed in segment 19 increases, the latter explanation is more consistent. This agrees also with expectations. As the radius increases, the path of the electrons becomes longer and they are more likely to be affected by the field distortions. The situation is reversed for holes. Their path shortens and their trapping becomes less probable.

In order to systematically study the radial dependence of charge trapping, truncated mirror pulses were methodically searched for. For all positions and selected alpha events, the pulses of the segment underneath the interaction zone were classified [18]. The fractions f_α^{pt} of pulses falling into six “pulse types”(pt), “mirror positive”, “mirror truncated positive”, “mirror negative”, “mirror truncated negative”, “normal collecting” and “no activity”, were calculated. Figure 9 shows f_α^{pt} as a function of the radius for the three different azimuthal angles associated with the scans RS01, RS02 and RS03. The results are very consistent at the different angles. Up to $r = 30$ mm, all events show positive truncated mirror-pulses, indicating hole trapping. At $r = 34$ mm, the fractions of positive truncated mirror-pulses drops and negative truncated mirror-pulses become observable. At the edge of the detector, negative truncated mirror-pulses dominate, indicating electron trapping. The radial dependence of the effect is the same for RS02 close to the metalisation as for the other scans.

The results obtained for the two azimuthal scans AS01 and AS02 at $r = 26$ mm and $r = 30$ mm confirm the results of the radial scans. For both scans, 100% of the events contain positive truncated mirror-pulses in the respective segments underneath segment 19.

Truncated mirror pulses were also searched for in gamma events at the scan positions where alpha events were observed. None were found. This confirms that charge trapping is restricted to charge carriers created very close to the surface.

The observed energies in the core and segment 19 were converted to “effective thicknesses”, DL_i^{eff} , of the effective dead layer as

$$DL_i^{\text{eff}} = \left(\frac{dE}{dx} \right)^{-1} (E^{\text{ini}} - \mu_i) , \quad (2)$$

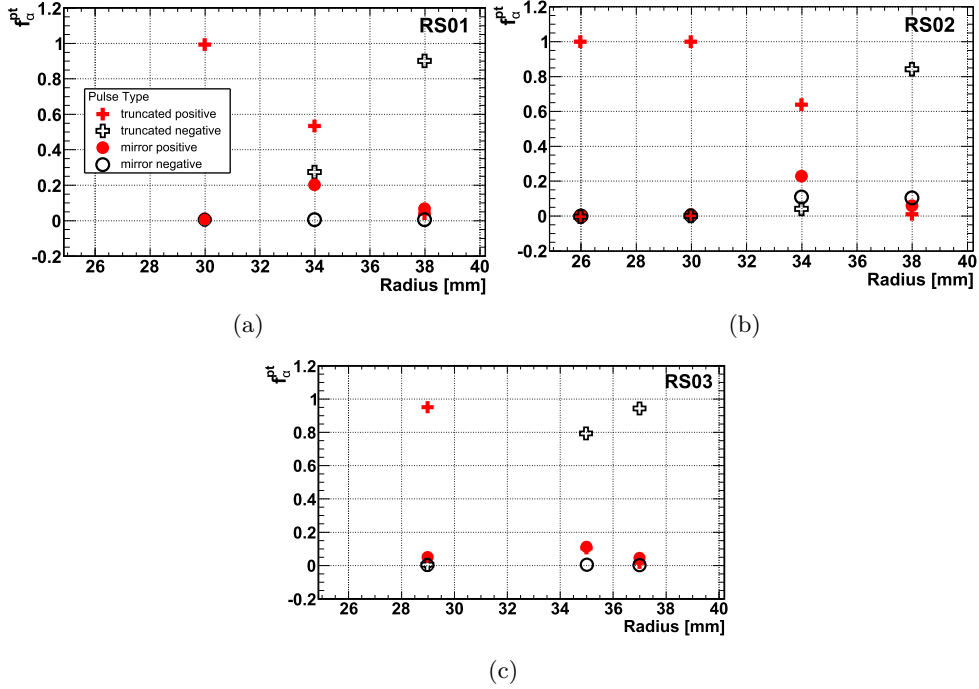


Figure 9: f_{α}^{pt} as a function of the radius for different azimuthal angles: (a) $\phi = 33^\circ$, RS01, (b) $\phi = 312^\circ$, RS02, (c) $\phi = 176^\circ$, RS03, adapted from [18].

where $i = 0$ or 19, E^{ini} is the average incident alpha energy and μ_i is the observed average energy for the selected alpha events. This assumes that the energy observed is related to the energy lost in an inactive volume of the detector. This is clearly not the case as energy is also lost due to charge carrier trapping. However, for an experiment which only records energies, this is a convenient and common nomenclature. The results are depicted in Fig. 10.

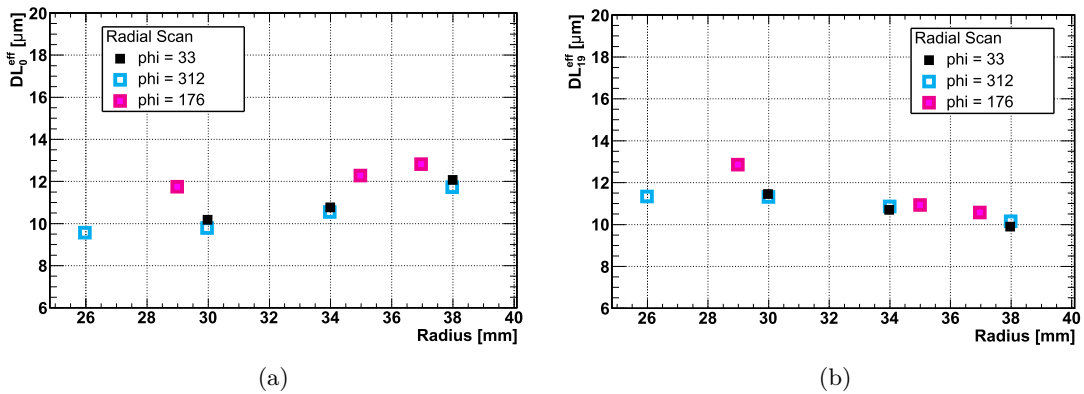


Figure 10: Effective dead layer thicknesses, DL_i^{eff} , as a function of the radius for (a) the core, $i = 0$, and (b) segment 19, $i = 19$. The statistical uncertainties as determined by the fitting procedure are smaller than the symbol size, adapted from [18].

Corresponding to the decrease of observed energy in the core at increasing radii, DL_0^{eff} slightly increases, see Fig. 10(a). The situation for the holes, see Fig. 10(b), is reversed. The conditions are very similar for all three radial scans. At $\phi = 176^\circ$, the values of DL_0^{eff} and DL_{19}^{eff} at $r = 29$ mm are slightly larger than for the other locations. This area is far away from the metalisation. However, the area covered by the azimuthal scan AS01 from $\phi = 95^\circ$ to $\phi = 130^\circ$ at $r = 26$ mm is equally

far away from the metalisation and does not show thicker effective dead layers. The values are $DL_0^{\text{eff}} \approx 10 \mu\text{m}$ and $DL_{19}^{\text{eff}} \approx 12 \mu\text{m}$ and are quite constant, see Fig. 11(top row).

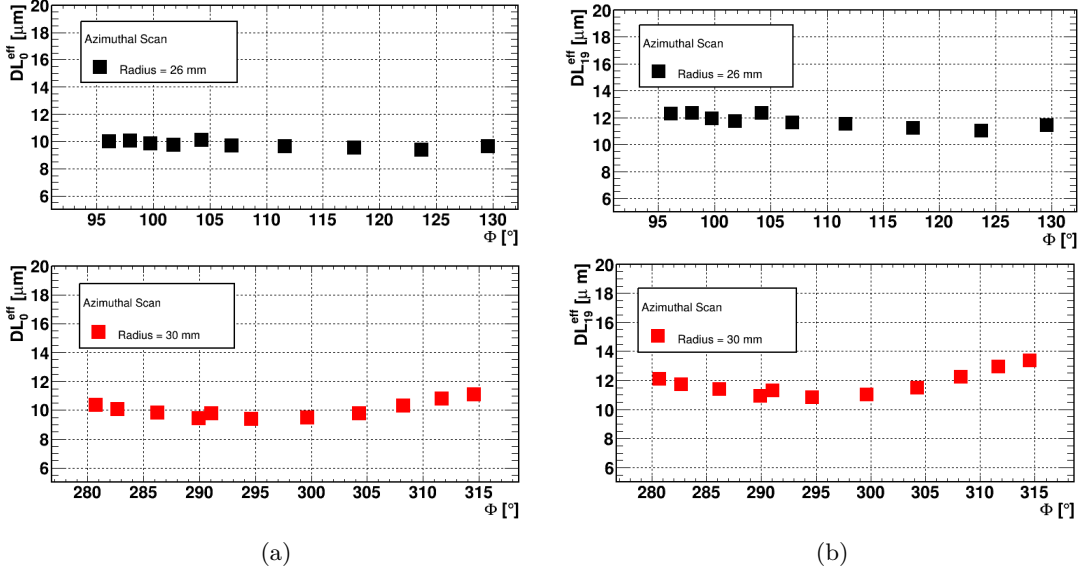


Figure 11: Effective dead layer thicknesses, DL^{eff} , as a function of the azimuthal angle for (a) the core, $i = 0$, and (b) segment 19, $i = 19$. The statistical uncertainties as determined by the fitting procedure are smaller than the symbol size, adapted from [18].

The scan AS02, close to RS02 and covering the metalisation at $r = 30 \text{ mm}$, revealed a shallow dependence on ϕ of both DL_0^{eff} and DL_{19}^{eff} , see Fig. 11(bottom row). At the centre of the metalisation, both drop to about $10 \mu\text{m}$. It should be noted again that DL_0^{eff} and DL_{19}^{eff} are just a convenient nomenclature. The drop is more likely due to less charge trapping. The smallest value of DL_0^{eff} could indicate a truly dead layer. But this is also rather unlikely. In Figs. 4(b) and 8, events with observed energies in the core and segment 19 well above the alpha peaks are visible. Thus, there are events in which the charge carriers escape and make it all the way to the electrodes. On the other hand, the bands also extend to very low observed energies. For these events, almost all charge carriers cannot be collected, even though they were generated down to $26 \mu\text{m}$. The events in the observed alpha peaks are very reproducible. However, the other events cover a large phase-space of observed energies.

In general, the situation is quite similar at all locations where alpha interactions were observed. Alpha-dedicated measurements were also performed at radii smaller than 25 mm , see Fig. 2(b). However, alpha peaks were not observed anywhere for these smaller radii. The thickness of the inactive volume of the detector is rapidly growing in this region. This was also previously observed by probing with low energy gammas [20].

6. Risetimes of pulses

The risetime of pulses, RT_i^{10-90} , presented and discussed here always denotes the time in which the pulse rises from 10% to 90% of its amplitude. As the pulses recorded for the core are very different than for segment 19, this results in very different risetimes. The distributions of the risetimes for the radial scan RS01 are shown in Fig. 12.

The pulses recorded in segment 19 rise much slower than the core pulses. This is possible because the holes drifting close to the mantle contribute little to the core pulse as the core weighting field is small in this region. The pulses in segment 19 are extremely long. The length of the expected drift path does not seem to be the determining fact, but rather the passage through a volume where the electric field lines are extremely distorted and the holes drift slowly. The

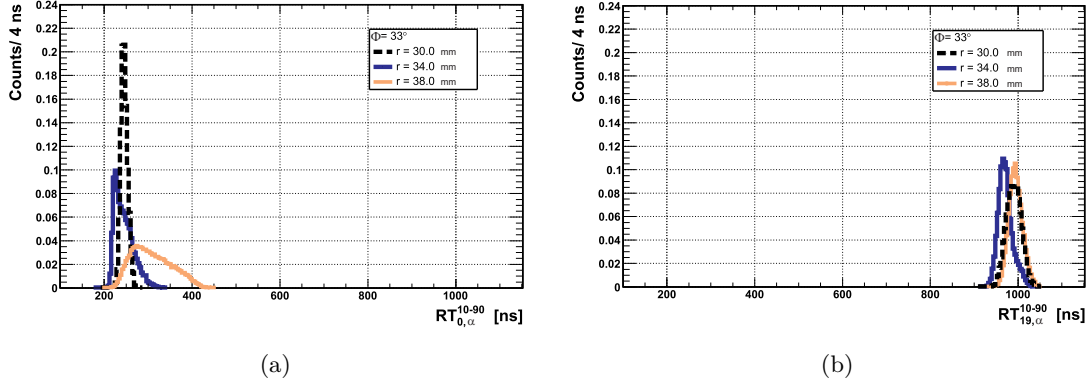


Figure 12: Distribution of risetimes (a) RT_0^{10-90} for the core and (b) RT_{19}^{10-90} for segment 19 for the radial scan RS01, adapted from [18].

situation is different for the core pulses. They get longer for larger radii in accordance with the longer drift path.

The mean values of the risetime distributions of alpha events are shown for the two azimuthal scans in Fig. 13(a). The core pulses have average risetimes of slightly less than 300 ns for both scans. The average risetimes of the segment 19 pulses are however very different for the two scans. In the sector around the metalisation, the segment 19 pulses rise almost as fast as the core pulses. This indicates that the electric field is significantly less distorted in the sector with the metalisation than in the other sectors.

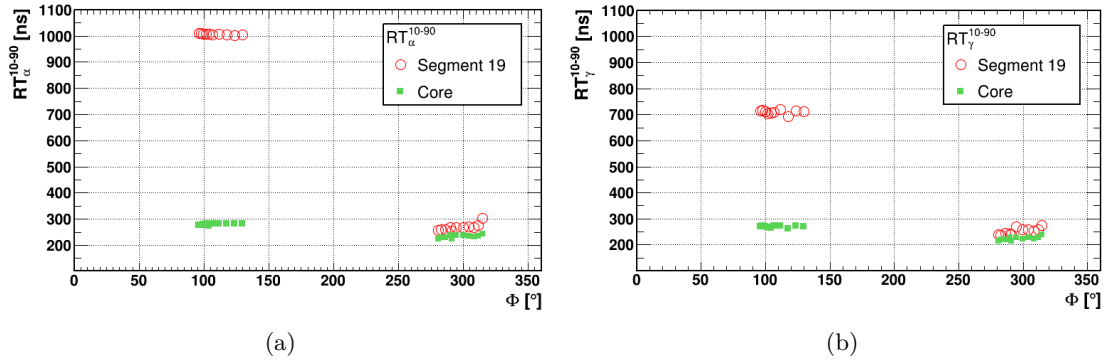


Figure 13: Azimuthal dependence of the average RT^{10-90} for the core (square) and segment 19 (open circle) for (a) selected alpha events, (b) 59.5 keV gamma events.

Figure 13(b) shows the average risetimes for 59.5 keV gamma events. These gammas almost probe the complete volume of the top segment. Some gammas interact close to critical areas of the detector, where the charge collection is extremely slowed down. Some gammas, however, interact far away from such critical area. This causes extremely broad risetime distributions. The mean of these distributions lies significantly above the mean of the core distributions for the sector far away from the metalisation. This indicates that the distortion of the field is not restricted to the very thin layer probed by alpha particles.

This is confirmed by a side-scan of segment 19 which was performed earlier [20] in the K1 [19] vacuum cryostat. A 42 kBq collimated ^{152}Eu source was rotated around the detector at $z = 67.5$ mm, the middle of segment 19 (see 2(c)), in steps of about 10° . Single-segment 19 events with an energy of 121.78 ± 5 keV, corresponding to a strong gamma line of ^{152}Eu , were selected. The mean free path of such gammas is about 4 mm and the dominant interaction cross section is associated to the photo effect. Thus, most interactions create a single energy deposit close to the

outer mantle.

Figure 14 shows the mean risetimes for (a) the core and (b) segment 19. Again, the difference is striking. While the core pulses show the normal small variation in risetime depending on their relative location to the crystal axes, the segment 19 pulses only show “normal” risetimes close to the metalisation. For locations far away from the metalisation, the risetimes are as large as for the alpha induced events. This proves that the effect of the missing metalisation is not confined to the very top of segment 19.

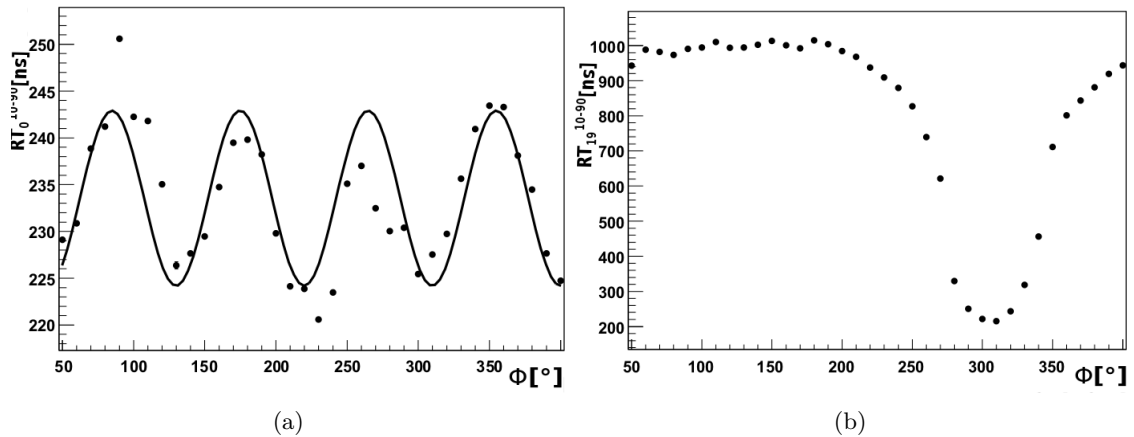


Figure 14: The mean RT_i^{10-90} (a) for the core, $i = 0$, and (b) for segment 19, $i = 19$ as a function of ϕ as determined from a side-scan of the detector, adapted from [20].

7. Conclusions

The observation of alpha events over most of the surface of the passivated end-plate of a true-coaxial detector was not really expected. It demonstrates that the effective dead layer underneath the passivation layer is extremely thin, only of the order of $10 \mu\text{m}$ thick. The spectra resulting for alpha interactions in the end-plate cover the region around 2 MeV where the signal for neutrinoless double beta decay would appear. If only the energy registered in core is recorded, such an alpha event could be mistaken for a signal event. A simple analysis of the shape of the core pulse would not help, because its risetime is normal.

In order to identify such events on the surface of an end-plate, it is necessary to read out the mantle. The difference between the energies recorded for the core and the mantle can tag alpha induced surface events.

Surface events are characterised by charge trapping, both of holes and electrons. However, to clearly identify these trapping effects, it is necessary to have the mantle segmented. This might not be favourable for a large scale experiment with hundreds of detectors. A possible handle might be a special configuration of the metalisation close to the end-plate. Contrary to intuition, it might be favourable to leave a small ring of the detector close to the end-plate without metalisation. A ring height of 5 mm is definitely too much because it affects an equally deep layer, but a ring height matching the volume to be tagged could help to identify events close to the end-plate through the slow rise of their mantle pulses.

Acknowledgements

We would like to thank the staff of Canberra France, now Mirion technology, for their cooperation.

References

- [1] I. Abt, et al., A New Ge^{76} Double Beta Decay Experiment at LNGS: Letter of Intent [arXiv:hep-ex/0404039](#).
- [2] N. Abgrall, et al., The Majorana Demonstrator Neutrinoless Double-Beta Decay Experiment, *Adv. High Energy Phys.* 2014 (2014) 365432. [arXiv:1308.1633](#), [doi:10.1155/2014/365432](#).
- [3] Neutrino 2016: First results from GERDA Phase II, http://neutrino2016.iopconfs.org/IOP/media/uploaded/EVIOP/event_948/09.25_5__agostini.pdf (2016).
- [4] S. R. Elliott, et al., Initial Results from the MAJORANA DEMONSTRATOR, 2016. [arXiv:1610.01210](#). URL <https://inspirehep.net/record/1489627/files/arXiv:1610.01210.pdf>
- [5] F. Feruglio, et al., Neutrino oscillations and signals in β and $0\nu\beta\beta$ experiments, *Nucl. Phys. B* 637 (2002) 345. [arXiv:hep-ph/0201291](#).
- [6] W. Maneschg, Review of neutrinoless double beta decay experiments: Present status and near future, *Nucl. Part. Phys. Proc.* 260 (2015) 188 – 193. [doi:http://dx.doi.org/10.1016/j.nuclphysbps.2015.02.039](#).
- [7] C. Aalseth, et al., CoGeNT: A Search for Low-Mass Dark Matter using p-type Point Contact Germanium Detectors, *Phys. Rev. D* 88 (1) (2013) 012002. [arXiv:1208.5737](#), [doi:10.1103/PhysRevD.88.012002](#).
- [8] K.-J. Kang, et al., Introduction to the CDEX experiment, *Front. Phys. China* 8 (2013) 412–437. [arXiv:1303.0601](#), [doi:10.1007/s11467-013-0349-1](#).
- [9] F. Ruppin, J. Billard, E. Figueroa-Feliciano, L. Strigari, Complementarity of dark matter detectors in light of the neutrino background, *Phys. Rev. D* 90 (8) (2014) 083510. [arXiv:1408.3581](#), [doi:10.1103/PhysRevD.90.083510](#).
- [10] R. A. Johnson, T. H. Burritt, S. R. Elliott, V. M. Gehman, V. E. Guiseppe, J. F. Wilkerson, Alpha Backgrounds for HPGe Detectors in Neutrinoless Double-Beta Decay Experiments, *Nucl. Instr. and Meth. A* 693 (2012) 51–58. [arXiv:1201.0165](#), [doi:10.1016/j.nima.2012.06.043](#).
- [11] R. J. Dinger, Dead layers at the surface of p-i-n detectors - a review, *IEEE Trans. Nucl. Sc.* 22 (1975) 135.
- [12] H. Utsunomiya, et al., Surface channel effect on $\gamma\gamma$ -ray response functions of coaxial germanium detectors, *Nucl. Instr. and Meth. A* 548 (2005) 455 – 463.
- [13] J. Eberth, J. Simpson, From Ge(Li) detectors to gamma-ray tracking arrays: 50 years of gamma spectroscopy with germanium detectors, *Prog. Part. Nucl. Phys.* 60 (2008) 283–337. [doi:10.1016/j.ppnp.2007.09.001](#).
- [14] G. Maggione, et al., Characterization of different surface passivation routes applied to a planar hp-ge detector, *Eur. Phys. J. A* 51 (2015) 141. [doi:10.1140/epja/i2015-15141-9](#).
- [15] B. Majorovits, et al., Aluminum as a source of background in low background experiments, *Nucl. Instr. and Meth. A* 647 (2011) 39–45. [arXiv:1105.3591](#), [doi:10.1016/j.nima.2011.05.042](#).
- [16] I. Abt, et al., The GALATEA Test-Facility for High Purity Germanium Detectors, *Nucl. Instr. and Meth. A* 782 (2015) 56–62. [arXiv:1409.0493](#), [doi:10.1016/j.nima.2015.02.007](#).
- [17] S. Irlbeck, The galatea test facility and a first study of α -induced surface events in a germanium detector, Phd thesis, Ludwig-Maximilians-Universität (March 2014). URL https://edoc.ub.uni-muenchen.de/17046/1/Irlbeck_Sabine.pdf
- [18] L. Garbini, Alpha-event characterization for germanium detectors, Phd thesis, Ludwig-Maximilians-Universität (May 2016). URL https://edoc.ub.uni-muenchen.de/19454/7/Garbini_Lucia.pdf
- [19] I. Abt, et al., Characterization of the first true coaxial 18-fold segmented n-type prototype detector for the GERDA project, *Nucl. Instr. and Meth. A* 577 (2007) 574–584. [arXiv:nuc1-ex/0701004](#), [doi:10.1016/j.nima.2007.03.035](#).
- [20] D. Lenz, Pulse shapes and surface effects in segmented germanium detectors, Phd thesis, Technische Universität München (March 2010). URL <https://mediatum.ub.tum.de/doc/969435/969435.pdf>
- [21] D. Gutknecht, private communication (2015).
- [22] M. Descovic, et al., Effects of neutron damage on the performance of large volume segmented germanium detectors, *Nucl. Instr. and Meth. A* 545 (2005) 199.